

Haris Moazam SheikhDepartment of Mechanical Engineering,
University of California, Berkeley,
Berkeley, CA 94720, USA
email: harisshikh@berkeley.edu**Sangjoon Lee**Department of Mechanical Engineering,
University of California, Berkeley,
Berkeley, CA 94720, USA
email: sangjoonlee@berkeley.edu**Jinge Wang**Department of Mechanical Engineering,
University of California, Berkeley,
Berkeley, CA 94720, USA
email: jinge@berkeley.edu**Philip S. Marcus¹**Department of Mechanical Engineering,
University of California, Berkeley,
Berkeley, CA 94720 USA
email: pmarcus@me.berkeley.edu

Airfoil Optimization using Design-by-Morphing

We present *Design-by-Morphing (DbM)*, a novel design methodology to create a search space for topology optimization of 2D airfoils. Most design techniques impose geometric constraints or designers' bias on the design space itself, thus restricting the novelty of the designs created, and only allowing for small local changes. We show that DbM methodology doesn't impose any such restrictions on the design space, and allows for extrapolation from the search space, thus allowing for truly radical and large search space with only a few parameters. We apply DbM to create a search space for 2D airfoils, and optimize this shape design space for maximizing the lift-over-drag ratio, CLD_{max} , and stall angle tolerance, $\Delta\alpha$. Using a genetic algorithm to optimize the DbM space, we show that we create a Pareto-front of radical airfoils that exhibit remarkable properties for both objectives.

Keywords: Design-by-Morphing (DbM), Topology Optimization, Airfoils

1 Introduction

Optimizing the shape of an airfoil is an integral design stage for aerodynamic components like aircraft wings[1–4] and wind-turbine blades[5–10]. A typical airfoil optimization process contains three main components: shape parameterization, airfoil evaluation, and optimization, among which the parameterization method determines both the design space and the complexity of the optimization problem. In this sense, a desirable parameterization technique must cover a wide design space within a limited number of design parameters[11–13], which is especially important during the early design stage when minimum geometric constraints are placed and radical changes during the optimization process are welcomed.

Different shape parameterization methods offer different fidelity and ranges of control[11,13], and, according to the scope of the design parameters, one can place these methods on a spectrum where, on one end, the change of one parameter affects only a local section of the airfoil shape thus offering a finer control of the shape, and, on the other end, each design parameter affects the airfoil's global contour[11].

On the local end of the spectrum is the **discrete method**[14], whose design parameters are exactly the discrete surface points that define the airfoil shapes. Because the displacement of each point can be adjusted, the design space is potentially limitless[15], and very fine local control as well as high fidelity can be achieved. However, to describe an airfoil shape accurately, a large number of surface points are needed, which increases the complexity of the optimization problem. Furthermore, to accommodate the large number of design variables, one usually uses gradient-based method to guide the optimization which is limited to small local changes and can easily get stuck at a local optimum.

Increasing the geometrical extent of each parameter's influence, one would find classical methods that determine the airfoil shape based on the regional features or the control points and perform curve-fittings of some kind. For example, the popular **parametric section (PARSEC) method**[16] uses eleven parameters that rep-

resent specific sectional features such as leading edge radius and upper and lower crest locations and approximate the airfoil surface using a 6th order polynomial. Another popular method would be the **Bézier parameterization**[17], which forms the upper and the lower surfaces of the airfoil through the Bézier curves defined by the pre-selected control points. Additionally, a combination of the two techniques, **Bézier-PARSEC parameterization**[18], also exists, which creates Bézier curves using the parameters of the PARSEC method and combines these curves to form the shape contours. One main issue with the above methods is their inability or inefficiency to include high-fidelity features: the PARSEC and the Bézier-PARSEC method have fixed number of parameters and offer very limited range of fidelity, while the Bézier parameterization requires higher-degree Bézier curves to describe complex shapes, which become inefficient to calculate as the order increases[15].

To include high-fidelity features, or, equivalently, represent more complex curves, **B-splines**[19,20], including **nonuniform rational B-spline (NURBS)**[21], can be used, which form curves by connecting low-order Bézier segments defined by the control points. Naturally, with denser control points, these methods move to the local end of the spectrum and are able to represent high-fidelity features, but the computation complexity also increases. In an effort to reduce the number of the design parameters, the control points can be grouped together, and global transformations such as twisting and thickening can be used as the parameters instead. This is known as the **free-form deformation (FFD) method**[22,23] and is closer to the global end of the spectrum. A similar method, namely **Radial Basis Function Domain Element (RBF) approach**[24,25], also exists and uses radial basis function to exert deformation on the airfoil.

To the global end of the spectrum includes methods that use spectral construction of some basis functions or modes to form or deform the airfoil shapes. One typical way of determining the basis modes is through **proper orthogonal decomposition (POD)** of a set of airfoil data, and dimensionality can be reduced by using only the dominant modes[26,27]. Other methods include the **Hicks-Henne's approach**[28], which uses a linear combination of sine functions to deform the airfoil surface, and **class/shape function transformation (CST) method** proposed by Kulfan[29,

¹Corresponding Author.

Version 1.18, July 26, 2022

30], which represents an airfoil shape as the product of a class function and a shape function formed by a linear combination of Bernstein polynomials. Similar to all the other methods on the spectrum, in order to resemble high-fidelity features, more basis modes have to be included, which again falls into the so-called the curse of dimensionality.

There have been attempts that aim to reduce the number of parameters needed while capturing a large enough design space[31–33]. A most recent one was conducted by Chen et al.[34], who used a deep generative model, called Bézier-GAN, to parameterize airfoil shapes by learning from the major shape variations in an existing database. Furthermore, they preserve the minor features of the airfoil shapes via a noise space, which allows them to separate the major and the minor features hence leading to a faster design space exploration. However, this study, like many other dimension reduction methods, relies on the assumption that the optimum design is not far from an existing database, which is not always true. For our study, we mainly consider the shape parameterization technique for the early design stage and prefer not to make the same assumption. In particular, We are interested in a method that would contain high-order features while keeping a limited number of design parameters and allowing radical change from the initial airfoil shapes.

In this paper, we apply the Design-by-Morphing (DbM) parameterization technique, a novel design strategy that was introduced by Oh et al.[35] and has been used in recent years for geometry optimization of different problems[35,36], to the airfoil optimization problem. Specifically, our DbM method ‘morphs’ the baseline shapes together to create new shapes and can interpolate as well as extrapolate the design space, which allows for both the high-fidelity representation of shapes without the curse of dimensionality and radical improvements in the shapes without any geometric constraints[35]. Our paper makes the following scientific contributions:

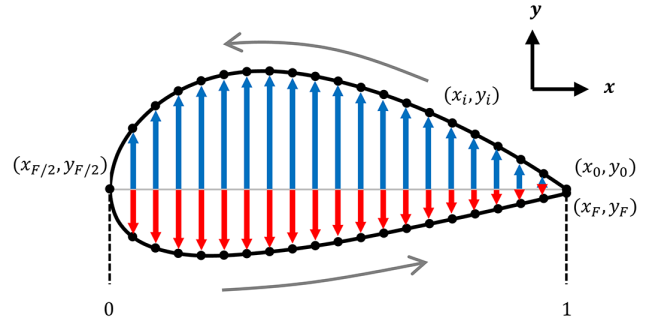
- A DbM parameterization technique designed for the two-dimensional airfoil shape optimization allowing both accurate reconstruction of the existing airfoil database and radical change of airfoil shapes while being free of geometric constraints and designers’ biases.
- An optimization strategy using the DbM parameterization technique and the genetic algorithm that is able to create the Pareto-front of multi-objective airfoil optimizations.

2 Design-by-Morphing

Design-by-Morphing (DbM) works by morphing homeomorphic, i.e. topologically equivalent, shapes to create a continuous and constraint-free design search space that can produce radical extrapolated shapes, something which is unique from existing design strategies. The details of DbM are presented in the subsequent subsections.

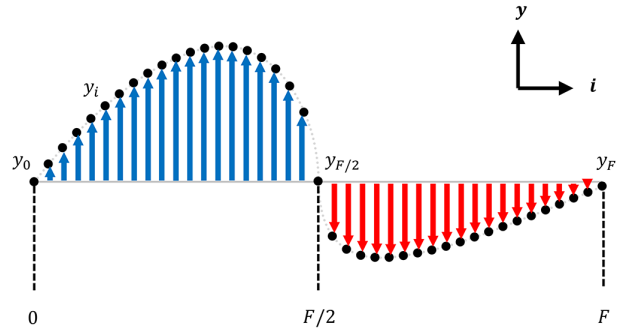
2.1 Baseline Shapes and Morphing. The DbM technique generally requires two or more ‘baseline shapes’, usually chosen from pre-existing designs in the literature, for the design search space creation. In order to be ‘morphed’ together, these baseline shapes must be homeomorphic, which can be achieved by establishing a one-to-one correspondence between the shapes via some systematic shape collocation methods in either the functional[35] or geometric space[36]. The new shapes can then be generated by applying weights to the baseline shape collocation vectors and summing them together.

The DbM method is valid for shapes of any dimensions, and because radically different baseline shapes can be morphed together, exotic shapes can be created. Furthermore, in addition to ‘interpolation’ between the shapes, applying negative weights during morphing allows ‘extrapolation’ from the search space spanned by the baseline shapes, which can create truly novel and unusual



$$y(x_i) = y_i \quad (x_i = |1 - 2i/F|, \quad 0 \leq i/F \leq 1)$$

(a) n^{th} airfoil shape



$$\mathbf{S}_n = [y_0, y_1, \dots, y_F]$$

(b) y -coordinate collocation vector

Fig. 1 An example of DbM. The coordinates of the baseline shapes are weighted, summed, and normalized to form the coordinates of a morphed shape.

shapes. Lastly, DbM is completely free from any geometric parameter constraints and the only implicit constraints are the selections of the ‘baseline shapes’ themselves.

For 2D airfoils, the closed shapes can be collocated in the Euclidean coordinate system. We note here that all 2D shapes bounded by a single surface are homeomorphic to one another. Using the leading edge of each airfoil as origin, each shape can be collocated by taking fixed and uniformly spaced points on the x -axis, which creates a one-to-one correspondence between the shapes. This collocation strategy is demonstrated in Figure 1, and the baseline shapes used in this paper are chosen from various airfoils from literature, which are detailed later. Morphing is performed by multiplying a specific airfoil shape with a scalar weight, summing up the weighted vectors, and then normalizing them, which is given by Eq. 1:

$$\mathbf{P}(\mathbf{x}) = \frac{1}{\sum_{m=1}^N w_m} \sum_{n=1}^N w_n \mathbf{S}_n(\mathbf{x}). \quad (1)$$

Here $\mathbf{S}_n(\mathbf{x})$ is the y -coordinate collocation vector determining the n^{th} baseline shape, collocated at $\mathbf{x} = [x_0, \dots, x_F]$ where the i^{th} x -coordinate $x_i = |1 - 2i/F|$ and F is the number of collocation points. Accordingly, the first half elements of \mathbf{S}_n represents the top surface of the airfoil and the second half elements of \mathbf{S}_n renders the bottom surface of the airfoil. N is equal to the total number of baseline shapes. $w_n \in [-1, 1]$ is the morphing weight applied to the y -coordinate vector of the n^{th} baseline shape. A visual demonstration of our strategy is presented in Figure 2.

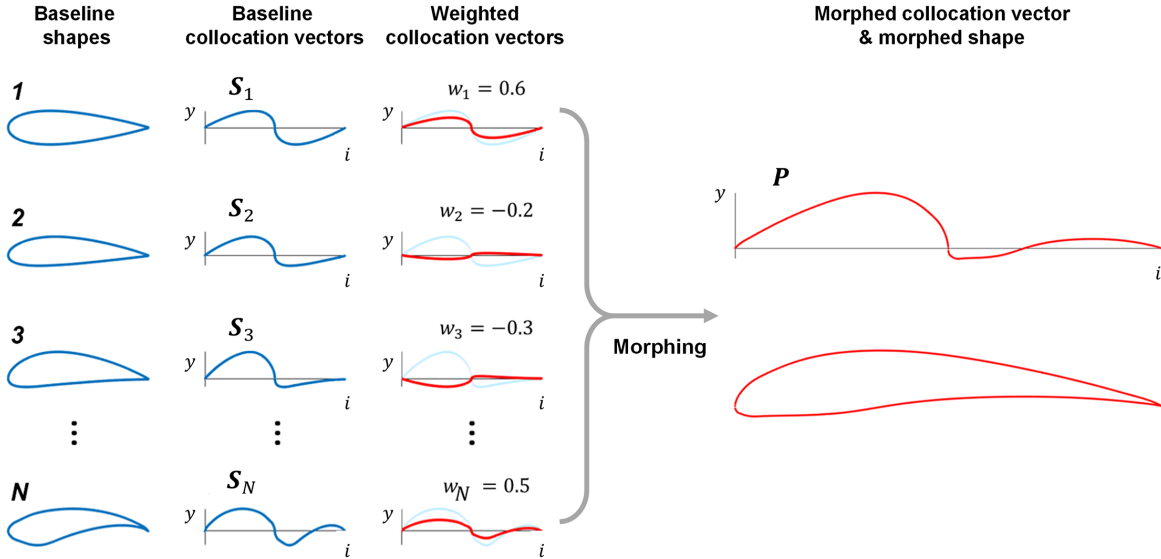


Fig. 2 An Example of DbM. Column 1 shows the baseline shapes. Column 2 depicts the elements of the collocation vectors of the baseline shapes plotted as a function of the index i of the collocation vector. Column 3 shows the weighted elements of the collocation vector plotted as a function of the index i of the collocation vector. Column 4 shows the resultant collocation vector of the morphed shape and the morphed shape itself.

2.2 Intersection Control. For smooth baseline shapes, applying positive weights, i.e. interpolation, will always create smooth shapes without applying any geometric constraint. However, because the DbM imposes no geometric parameter restraints, extrapolation, i.e. applying negative weights, may produce non-physical geometries such as self-intersections, which have ‘zero-area’ regions as shown in Figure 3(a). One may discard the morphed airfoil shapes with self-intersections during the optimization but that diminishes the size of our design space. Instead, we recover new shapes by removing the intersections. This is accomplished by first locating within the morphed coordinate vector where the intersection occurs and restructuring the coordinate vector by ‘flipping’ it between the intersection points as shown in Figure 3(c). The vector is then ‘stiffened’ to remove the zero area between the intersections by removing the points in their neighborhoods and then linearly interpolating between the broken coordinate vectors. As seen in Figure 3(d), this removes the ‘zero-area’ space and gives some physical area to the shape at the point of intersection. The above process is repeated until all intersections are removed, e.g. both intersections in Figure 3 are successfully removed, and, finally, a moving-average smoothing filter is applied to smooth out the sharp edges.

2.3 Baseline Shape Selection. The selection of baseline shapes is an important component of DbM strategy and ultimately determines the size and the novelty of our search space. Metaphorically, the selection of the baseline airfoil shapes serves as the gene pool for the morphed airfoils, and its diversity is important for creating a large design space. Our baselines shape selection contains good ones with either high lift-to-drag ratio or good stall performance, bad ones with poor aerodynamic performance, commonly used airfoil shapes in the literature or industry, and airfoils with irregular shapes to provide novelty to the design space. It is worth noting that, contrary to the conventional airfoil optimization processes[37], we deliberately include the bad performers so that our optimization can suppress their features by assigning negative weights to the corresponding baseline shapes. Our results in later sections will demonstrate this in greater detail.

In this paper, we select 25 baseline shapes (see Figure 4) from the UIUC airfoil coordinates database[38]. The airfoils are selected to ensure diversity and to introduce radical features in the design

space. Their model names and characteristics are attached in Appendix B. Each airfoil shape is represented by 4000 coordinates that span from the first surface trailing edge around the leading edge to the second surface trailing edge with equally distributed x -coordinates parallel to the airfoil chord line of a unit length.

2.4 Representation Capacity. To examine the robustness and the extent of our design space generated by the morphing of only 25 airfoil baselines, we reconstructed the pre-existing 2D airfoil shapes archived in the UIUC airfoil database[38] via DbM. A total of 184 randomly-chosen airfoils are tested, which accounts for approximately 11% of the UIUC database as of 2022. All 184 airfoils were reconstructed to the same accuracy, and a random selection of 100 out of the 184 airfoils are shown in Figure 5.

For each airfoil, the shape was reconstructed by running a global optimization of the weight vector that minimizes the total area of the original and morphed shapes where one shape does not overlap with the other, e.g. the geometric XOR of 2 closed shapes. Note that the geometric XOR serves as a good measure of the similarity between 2 shapes since it gradually goes to zero as the shapes become identical to one another. As a result, all the test airfoils were successfully re-created by the morphing of only 25 baseline shapes with the areal difference of less than 0.01. It means the average error in y -coordinate is $<0.5\%$ since the airfoil chord is normalized as a unit length and the area is formed by 2 airfoil surfaces. This affirms that the current 25 baseline shapes are diverse enough to span the design space via DbM to explore airfoils in a universal manner.

Overall, by using only 25 dimensions, our DbM method is able to recreate the UIUC database airfoils with high fidelity, and it does not suffer from the ‘curse of the dimensionality’ compared to other techniques where the fidelity of the parametrization depends on the number of independent dimensions used. Moreover, DbM’s capability of creating exotic shapes via its extrapolation feature increases the chance to find novel solutions that are deviated from the previously-established space like the UIUC database. This exploration is essential especially for the airfoil design where the correlation between the geometric feature and the aerodynamic performance of an airfoil can be very non-intuitive, thus necessitating exploratory design spaces.

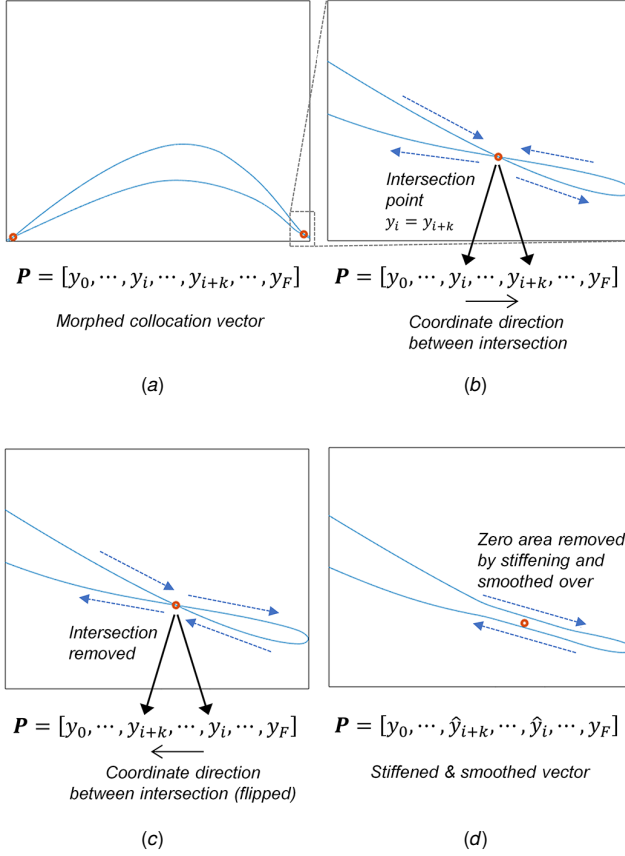


Fig. 3 Conditioning for intersection removal. (a) Intersections are detected; (b) Blown up image of one intersection. Shape coordinates direction is depicted by arrows; (c) Intersection removed by flipping vector between intersection; (d) Zero area removed by linear interpolation to remove the intersecting area and then smoothed over, shown by hat coordinates

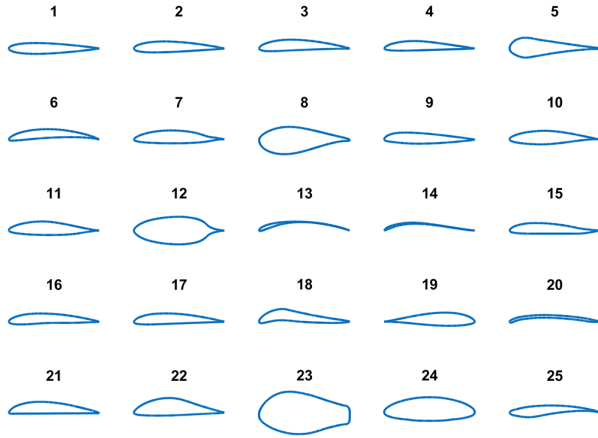


Fig. 4 Twenty-five baseline shapes picked from the UIUC airfoil coordinates database[38]. See Appendix B for more details.

3 Optimization Methodology

Our airfoil optimization methodology is built around the DbM technique introduced in Sec. 2. As shown by the flowchart in Figure 6, the optimization starts from the selection of the baseline shapes and then evaluates and optimizes the airfoils formed by

morphing these baseline shapes using DbM. Our methodology does not rely on one specific airfoil evaluation tool or one specific optimizer, and discussions on their choices are provided in Sec. 3.1 and Sec. 3.2 respectively.

3.1 Airfoil Evaluation. Our optimization methodology is not limited to one particular airfoil performance analyzer. One can use any CFD or experimental methods. For the optimization of airfoil shapes using CFD-based solvers, the evaluation of the objective functions (aerodynamic properties) typically falls into two categories: the full Reynolds-averaged Navier-Stokes (RANS) based approach and the interacted viscous/inviscid zonal approach. The RANS-based approach is computationally expensive and demands the optimizer to be highly efficient, and, to accommodate the large number of design variables as often seen in the aerodynamic designs, gradient-based optimizers coupled with adjoint methods for computing the derivatives are deemed the most feasible[39–41]. On the other hand, the viscous/inviscid zonal approach, which combines separate solutions for the inviscid external flow and the viscous shear layer flow iteratively to form a continuous profile, is faster and less expensive. Among the many inviscid/viscous airfoil analysis codes, the XFOIL program[42] has been the most dominant and widely adopted one[43–50]. It couples a vorticity panel method for exterior flow with an integral boundary-layer method for viscous boundary layers and uses an e^9 -type amplification formulation to determine the transition point[42]. Its applicability to airfoil designs has been demonstrated in the past literature, where its predictions of aerodynamic properties are shown in good agreement with the wind-tunnel experiment data[51,52] and the RANS-based simulation results[53].

The specific choice of the evaluation tool used in this paper is not essential to manifest the power of the DbM parameterization technique, which is the main focus of our paper. For this work, we opt for XFOIL because of its acceptable accuracy under our flow condition as well as its low computation cost. Its wide usage also allows quick reproduction of our optimization results. It is used in a black-box manner so that any other commercial or in-house airfoil analysis tools can be incorporated into our optimization framework if necessary. Our detailed airfoil evaluation setup is attached in the appendix B.

3.2 Optimization. When given a set of solutions, for single objective optimization problems, the most optimal solution within the set can be determined. However, for multi-objective optimization, multiple and potentially conflicting objectives must be considered simultaneously to determine the optimal answer in the solution set[54,55]. If the designer has a quantitative ranking of the objectives, these objectives can be combined together to formulate a single objective problem, but when no such ranking exists, constructing a Pareto front is the most common methodology[56–58], which is applicable to real-world problems such as the design of architected materials[59,60], turbo-machinery[61–65], process-engineering[66–68], shape design[69–71], and structural engineering[72,73] when multiple objectives that cannot be quantitatively ranked are involved.

We pose the multi-objective optimization problem as

$$w_{opt} = \underset{w \in \mathcal{W}}{\operatorname{argmax}}(f(w)), \quad (2)$$

where $f(w) = [f_1(w), f_2(w), \dots, f_K(w)]$. Here f_1, \dots, f_K are the K objectives to be maximized and w is the design variable vector. Generally w is a d -dimensional vector defined over a bounded set $\mathcal{W} \subset \mathbb{R}^d$ representing d continuous variables. $\{w_{opt}\}$ is a set of Pareto-optimal solution vectors, i.e., a vector which is not Pareto-dominated by any other vector. For the reader's convenience, it is noted that a design variable vector \hat{w} is Pareto-dominated by another design variable vector \tilde{w} if $f_k(\hat{w}) \leq f_k(\tilde{w})$ for all

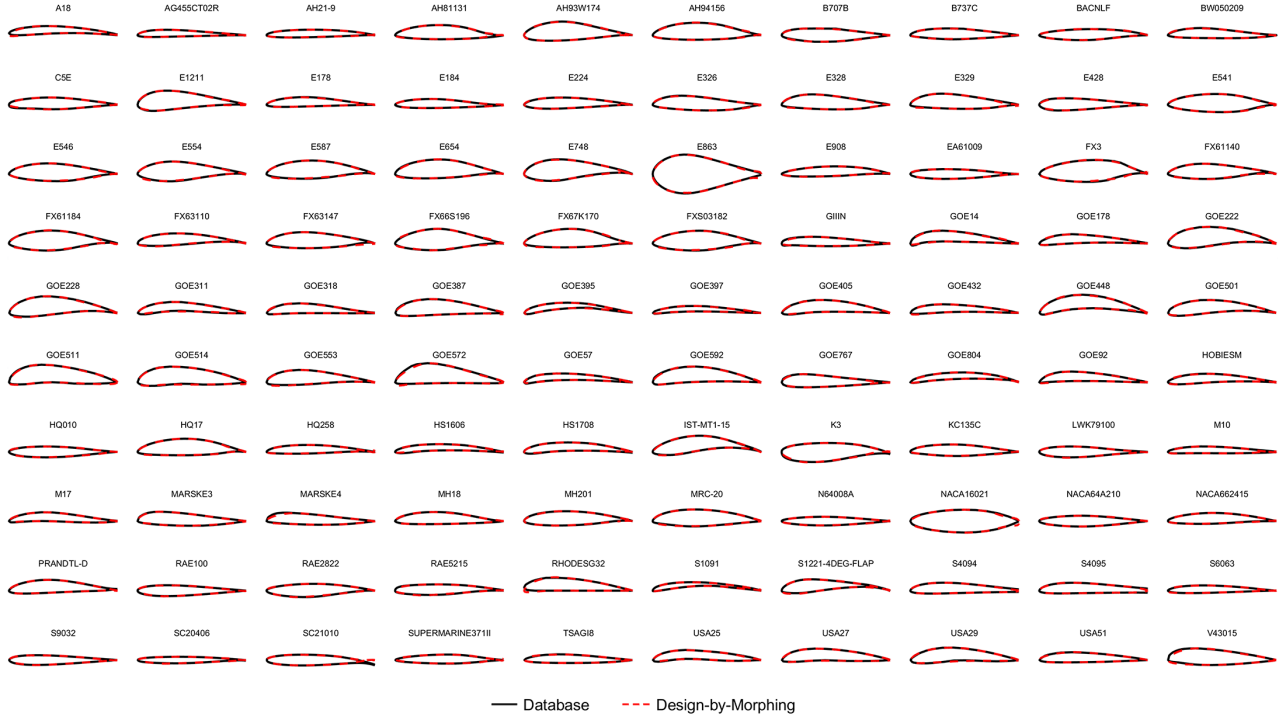


Fig. 5 Reconstruction of randomly chosen 100 pre-existing airfoil shapes via DbM using twenty-five baseline shapes in Figure 4.

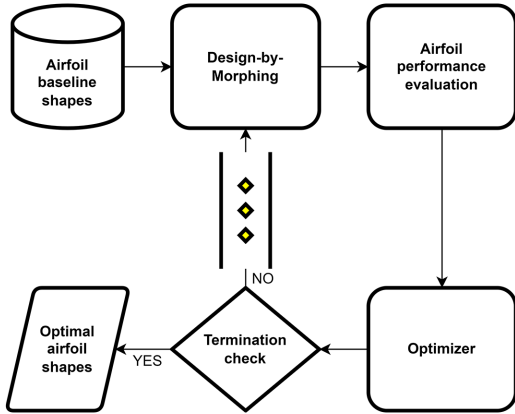


Fig. 6 General flowchart of airfoil optimization via DbM

$k \in \{1, \dots, K\}$. To obtain the Pareto-front, especially when objectives cannot be weighted or when a non-convex black-box function is considered, evolutionary or genetic algorithms are a natural choice[68,74]. In fact, they have been commonly implemented in many previous aerodynamic optimization studies due to their gradient-free nature and wide region of the search domain[30,75–77]. On the other hand, when the cost functions are expensive to compute (e.g. when using experiments as an evaluation tool), Bayesian optimization methods have proven to be efficient[78].

Our study considers a bi-objective ($K = 2$) two-dimensional airfoil shape optimization. In particular, we optimize the shape of a subsonic airfoil operating in an incompressible flow with $Re \equiv Uc/\nu$ of 1×10^6 , where U and ν are the free-stream flow speed and fluid kinematic viscosity, respectively, and c is the airfoil chord length. The parameter to be optimized is the morphing weight vector for the DbM technique:

$$\mathbf{w} \equiv (w_1, \dots, w_{25}) \in \mathcal{D}^{25}, \quad (3)$$

where $\mathcal{D} = [-1, 1] \subset \mathbb{R}$ and w_i ($i = 1, 2, \dots, 25$) is the weight applied to the i^{th} baseline shape. The design objectives to be maximized are the maximum lift-drag ratio at any angle of attack α , i.e. $f_1(\mathbf{w}) = CLD_{max}(\mathbf{w})$, and the difference between the stall angle α_s and the angle where the maximum lift-drag ratio occurs, i.e. $f_2(\mathbf{w}) = \Delta\alpha(\mathbf{w})$, where $\Delta\alpha$ is often called the stall angle tolerance. Precise definitions of these design objectives are explicated in Appendix A, and both objectives are evaluated using the XFOIL simulations, which are efficient enough to be used with the genetic algorithm.

We use a MATLAB-based variant of the popular NSGA-II[79] algorithm, which is a controlled, elitist genetic algorithm. Our initial population consists of the single-objective optimums of each design target as well as random samples in the design space. The population size of 372 is used with a total of 3,000 maximum generations, and the solutions are actively ranked within each generation so as to maintain diversity and avoid over-crowding in the Pareto-optimal solution set. Our setup was tested on the commonly used set of ‘ZDT’ benchmark problems for multi-objective problems, suggested by Zeidtlar et al.[80]. The details of the test problems and the validation results are provided in Appendix C.

4 Results

The Pareto front on the $\Delta\alpha - CLD_{max}$ objective plane, which resulted from the 3,000 generation genetic algorithm (GA) runs, is depicted in Figure 7. The convergence of the front is confirmed by the large generation number with the population size of 372, involving around 1.1 million XFOIL evaluations of CLD_{max} and $\Delta\alpha$. After non-dominant or duplicate individuals are removed in the final generation of the population, we are able to identify 208 Pareto-dominant airfoil shapes composed via DbM using 25 baseline airfoil shapes. For comparison, these 25 baseline shape cases are evaluated and plotted as red hollow circles in Figure 7 together. The reason why baseline #19 has zero CLD_{max} and $\Delta\alpha$ is that we inverted the shape intentionally and therefore XFOIL failed to evaluate its aerodynamic performance. We assigned the objective functions zero values for such failing cases because they represented

airfoil geometries that are not aerodynamically viable in the XFOIL space. The GA optimization successfully developed the Pareto front, where two ends are posed at $(CLD_{max}, \Delta\alpha) = (30.63, 40^\circ)$ and $(CLD_{max}, \Delta\alpha) = (273.39, 10^\circ)$. Even in the largest maximum lift-drag ratio case, the angle of attack gap between stall and design point is found to be 10° , giving the airfoil a tolerant range for off-design operations.

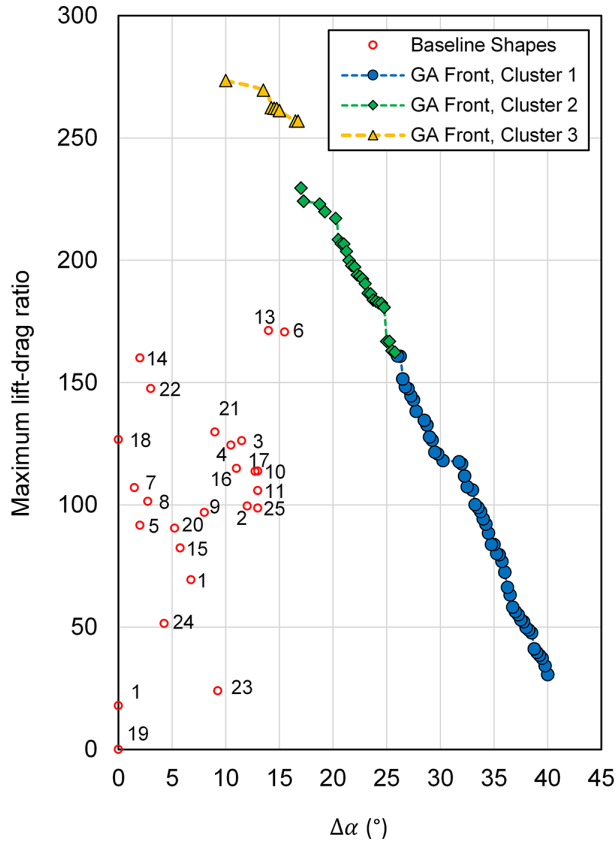


Fig. 7 The Pareto front consisting of the optimal airfoil shapes as a result of the 3,000 generation runs of NSGA-II. Twenty-five red hollow circles with indices indicate twenty-five baseline airfoil shape evaluations. See Appendix D to understand how the clustering is performed.

The front is divided into 3 different clusters, each of which constitutes a segment of the front which does not overlapping one another. It is worth noting that the non-overlapping division of the front is a consequence of clustering through the Principal Component Analysis (PCA), rather than arbitrary. The detail of the clustering is provided in Appendix D.

Figure 8 shows nine representative optimal airfoil shapes on the Pareto front in ascending order of CLD_{max} . In each cluster, three airfoil shapes having considerably different objective function values were selected to be presented. Also, note that Figure 8(a) illustrates the extreme case of the smallest CLD_{max} and largest $\Delta\alpha$ while Figure 8(i) depicts the other extreme of the largest CLD_{max} and smallest $\Delta\alpha$. It can be seen that within the cluster the overall shape remains identical and only a gradual decrease in the airfoil thickness is observed as CLD_{max} increases. Since thin airfoils such as bird-like airfoils[81], which we take as part of the baseline shapes, e.g. #13 and #14, are known to have high CLD performance, the trend of airfoil thickness observed in the Pareto front appears to be reasonable.

In cluster 1 where 112 optimal airfoil shapes exist, it is found that they mostly look similar to the total mean airfoil shape (see Figure 10(a)). This makes sense because they account for the

majority of the airfoil shapes located on the front. Moreover, this cluster is located near the origin in the PCA-projected weight space (see Figure 13 in Appendix D), indicating that there was no radical morphing of the airfoil shape taking place from the mean shape.

Next, cluster 2 contains 83 optimal airfoil shapes. Compared to the airfoil shapes in cluster 1, the most distinguishing feature is that the trailing edge region becomes narrow. This creates the sharp trailing edge, which is generally favorable to obtain a lift increase. However, they are still not deviated far from the origin in the PCA-projected weight space, and their common shape mostly resembles the total mean airfoil shape.

Finally, 13 optimal airfoil shapes are discovered in cluster 3 from the optimization. This cluster includes the airfoil shapes experiencing more drastic morphing than those of in other cluster. It can be confirmed that they are the thinnest airfoils where the leading edge region's thickness is also diminished.

The mean weight distributions with respect to 25 original baseline shapes are given in Figure 9. Overall, the weight distributions of 3 clusters comply with the weight distribution of the total mean. It turned out that baseline shape #13 (model name: AS6097) is commonly the most significant one for morphing. Since this baseline shape is the best in CLD_{max} and the second best in $\Delta\alpha$ among 25 baseline shapes (see Figure 7), it was likely to survive in the GA runs over the generations against the selection pressure that only sorts out dominant individuals in terms of both CLD_{max} and $\Delta\alpha$. However, excellence in the objectives of an individual baseline shape does not necessarily guarantee its survival, which is the case for the globally best baseline shape #6 (model name: AH 79-100C), as an individual's superior 'phenotype' may be no longer revealed, or even suppressed after the morphing is done and all 'genes' are mixed with each other.

As we discussed from the examination of the morphed airfoil shapes, both cluster 1 and 2's mean weight distributions show no considerable difference from the total mean weight distribution. Through small shape variation from the total mean airfoil shape as in Figure 10(a), it is possible to reach these optima relatively easily. In contrast, cluster 3 has a number of weights that are quite different from the mean (e.g., #6 and #11) and substantial morphing would be required if one starts with the total mean airfoil shape.

In the context of the present study, each axis obtained by the PCA can be represented by a unique form of morphed airfoil shapes because 25 PCA coefficient vectors defined in the weight space \mathcal{D}^{25} are orthogonal to each other. These 25 new morphed airfoils span the whole design space and therefore serve as alternative baseline shapes in lieu of the original ones. More importantly, the dominance of the first 2 PCA axes with respect to the data point variance suggests that the major geometric feature of 208 airfoil shapes we found via the optimization is virtually generated by morphing of these two new airfoils. Small variance of a PCA axis indicates that the data points are not considerably deviated from their mean on the axis. In other words, the baseline shape corresponding to this PCA axis has a marginal impact on morphing the airfoil shape for optimization. Once we pick two baseline shapes from the first two dominant PCA axes, whose associated collocation vectors are say \mathbf{P}_1 and \mathbf{P}_2 , and use them to morph the airfoil shape obtained from the total mean of the Pareto-optimal weight vector set, which corresponds to the mean collocation vector \mathbf{P}_{mean} , we get better understanding of how the morphing, especially along each PCA axis, has an influence on major geometric changes in the optimal airfoil shapes. These airfoil shapes are depicted in Figure 10, where the black and red surfaces are generated from the first and second half of the collocation points, respectively. For example, we note that the orientation of two surface of \mathbf{P}_1 is flipped in comparison to that of \mathbf{P}_{mean} , meaning that the stronger the weight of PCA axis 1 in the positive direction is, the narrower a morphed airfoil shape is.

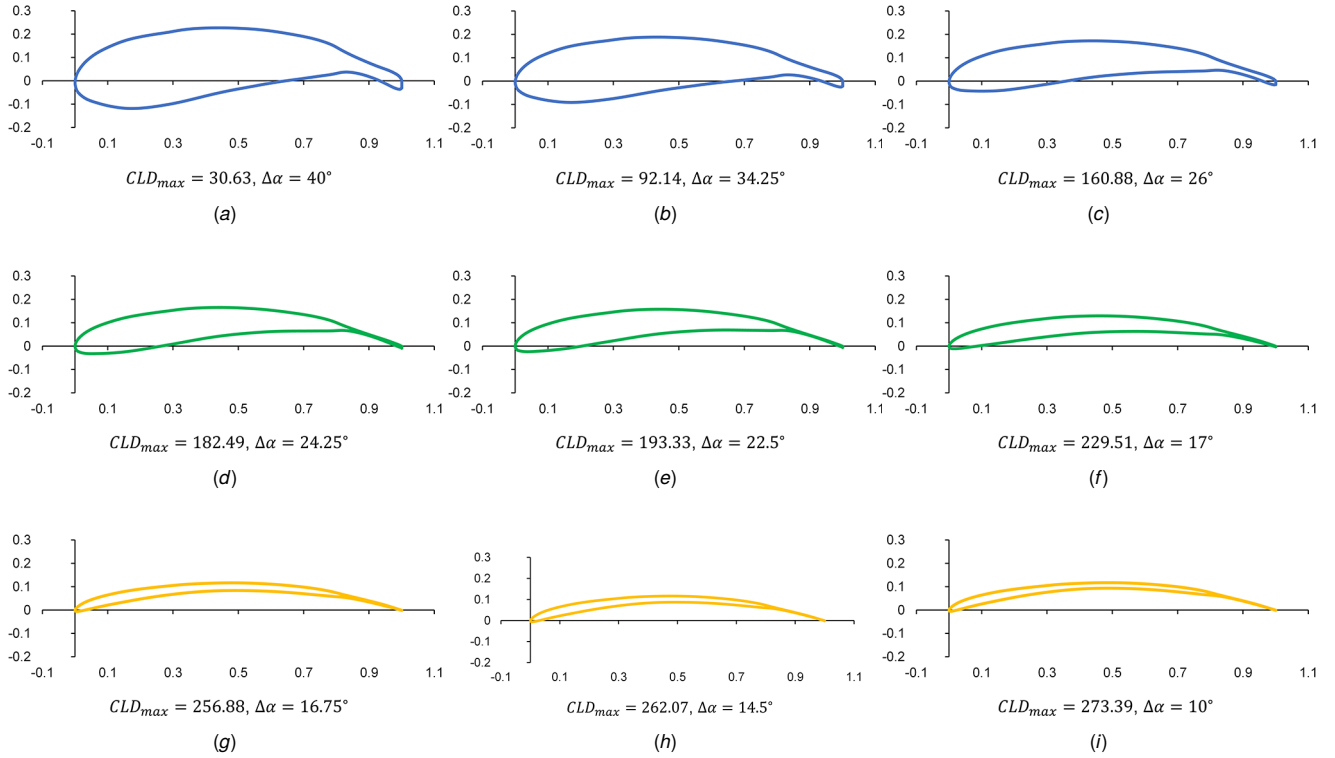


Fig. 8 Nine representative Pareto-optimal airfoil shapes. (a)-(c) are in cluster 1, (d)-(f) are in cluster 2 and (g)-(i) are in cluster 3.

5 Discussion

Most parameterization strategies depend upon careful selection of constraints and parameters, which determines their probability of success. The fidelity offered by such methods is very dependent on the number of the parameters chosen. Moreover, these designs are limited by the parametric constraints and the implicit designer's bias, making extrapolation or radical global changes difficult. Data driven methods typically rely on the assumption that the optimum solutions are not far from the training data-set, which again prevents radical shape changes.

Design-by-Morphing, on the other hand, creates a design space that is uninhibited by any geometric constraints and also allows extrapolation from the design space. It doesn't suffer from the curse of dimensionality when parameterizing airfoils and allows high-fidelity representation of airfoils without increasing the number of independent parameters in the problem. Using only 25 baseline shapes from the UIUC database, we were able to recreate the UIUC database with 0.5% error. We also showed that radical, global changes are possible using DbM. Applying that for the bi-objective shape optimization with objectives of maximizing CLD_{max} and $\Delta\alpha$, we were able to achieve significant results compared to our baseline shapes.

We posit that for design parametrization of airfoils and for other 2D/3D shapes, DbM should be the method of choice for creating an unconstrained, unbiased and non-data intensive design space that allows radical modifications, which can often be non-intuitive shapes.

6 Conclusion

DbM methodology creates a design space for radical 2D airfoils. We show that the space creates novel airfoils that are not constrained by geometric parameters or designer bias. Optimizing the design space created for dual objectives of CLD and $\Delta\alpha$, we show remarkable improvements in both objectives and provide a Pareto-front of optimal airfoil designs. Our final airfoils show

remarkable improvements over our existing baseline shapes. For optimizing 2D or 3D airfoils, DbM should be used as the method of choice for design space creation. Moreover, our methodology is flexible to be used for optimizing shapes for other fluid machinery as well. Currently we are applying DbM in tandem with Bayesian optimization for the optimization of 3D airfoils, vertical-axis wind turbines and draft tubes for hydro-kinetic turbines.

Acknowledgment

The authors would like to thank Dr. Ömer Savaş, affiliated with the Department of Mechanical Engineering, University of California at Berkeley for insightful discussions regarding airfoils and aerodynamics. The authors would also like to acknowledge that this work used the Extreme Science and Engineering Discovery Environment (XSEDE), which is supported by National Science Foundation grant number ACI-1548562 through allocation TG-CTS190047.

Funding Data

No funding was received for the undertaking of this project.

Data and Materials Availability

The data needed to evaluate the conclusions are present in the paper and Appendices. The data files and optimization setup will be posted in a public repository upon publication of the paper.

Nomenclature

- c = airfoil chord length (m)
- d = drag force of an airfoil per unit span (N m^{-1})
- l = lift force of an airfoil per unit span (N m^{-1})
- \mathbf{P} = y -coordinate collocation vector of a morphed airfoil
- \mathbf{S} = y -coordinate collocation vector of a baseline airfoil

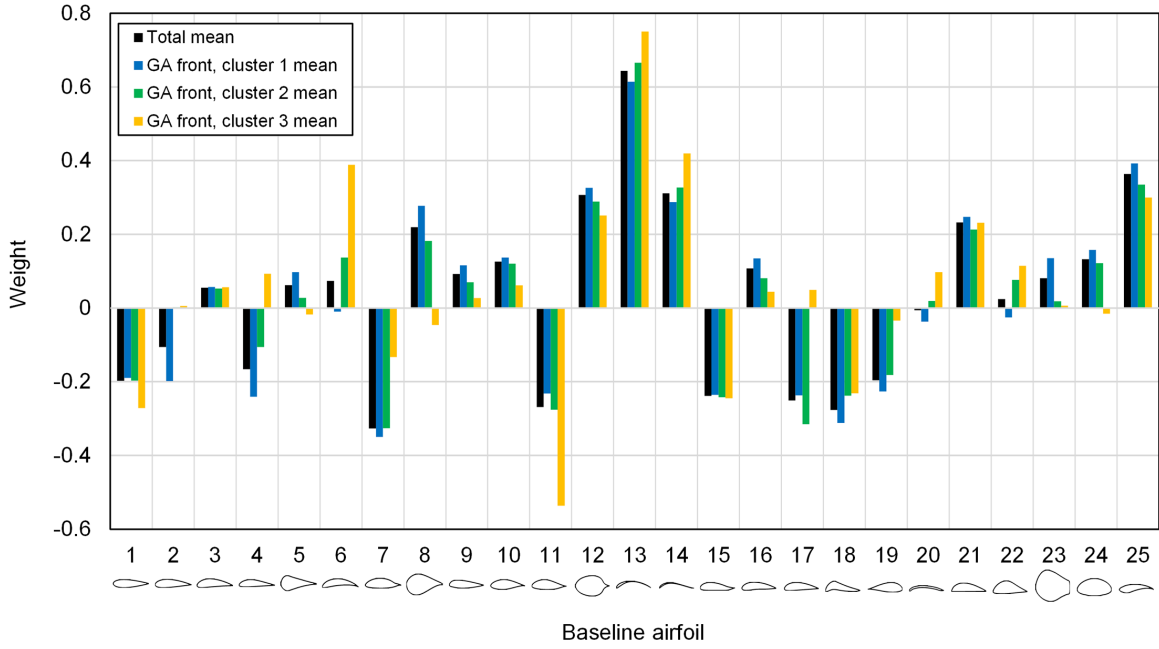
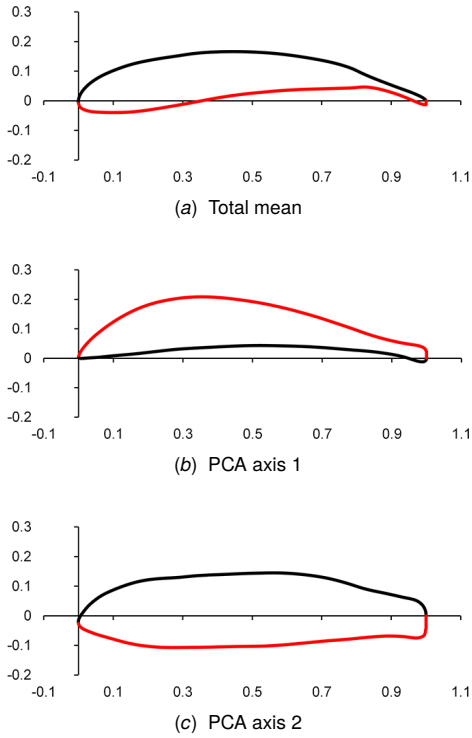


Fig. 9 Mean weight distributions of the Pareto-optimal airfoil shapes with respect to twenty-five baseline airfoil shapes.



Greek Letters

α = airfoil angle of attack ($^{\circ}$)

α_s = airfoil stall angle ($^{\circ}$)

$\Delta\alpha$ = stall angle tolerance, the range of α between the stall point and the maximum lift-drag ratio point ($^{\circ}$)

ν = fluid kinematic viscosity ($\text{m}^2 \text{s}^{-1}$)

ρ = fluid density (kg m^{-3})

Dimensionless Groups

C_d = drag coefficient of an airfoil per unit span, $2l/(\rho U^2 c)$

C_l = lift coefficient of an airfoil per unit span, $2d/(\rho U^2 c)$

CLD = lift-drag ratio of an airfoil, C_l/C_d

CLD_{max} = maximum lift-drag ratio of an airfoil, $\max_{\alpha} CLD(\alpha)$

Re = Reynolds number based on airfoil chord length, Uc/ν

Fig. 10 Morphed airfoil shapes generated by the optimal weight vectors, representing (a) the total mean of all optimal airfoils' weights, (b) the coefficients of the PCA axis having the most variance and (c) the coefficients of the PCA axis having the second-most variance. The black and red surfaces correspond to the first and second half of the collocation points, respectively.

U = free-stream flow speed (m s^{-1})

w = design-by-morphing weight factor

Appendix A: Aerodynamic Optimization Objectives

Airfoil optimization has become common in aerodynamic design problems involving maximization of one or more performance parameters of an airfoils. We mainly consider the following 2 performance parameters: the lift-drag ratio and stall angle. Given the flow speed U , fluid density ρ and airfoil chord length c , the lift and drag coefficients of an airfoil per unit span at an angle of attack α , C_l and C_d , are expressed as

$$C_l(\alpha) \equiv \frac{l(\alpha)}{\frac{1}{2}\rho U^2 c}, \quad C_d(\alpha) \equiv \frac{d(\alpha)}{\frac{1}{2}\rho U^2 c} \quad (\text{A1})$$

where l and d are lift and drag force per unit span, respectively, both of which change with respect to α . In this paper, these parameters are predicted via XFOIL[42], an program for analysis of subsonic isolated 2D airfoils, with varying α and then used for the optimization. Based on C_l and C_d , the lift-drag ratio CLD is calculated as:

$$CLD(\alpha) = \frac{C_l(\alpha)}{C_d(\alpha)}. \quad (\text{A2})$$

On the other hand, we define the stall angle α_s as an angle of attack where C_l reaches the first local maximum when we increase the angle starting from 0° , or

$$\alpha_s \equiv \min_{\alpha \geq 0} \alpha \quad \text{where} \quad \exists \delta > 0 \quad \text{such that} \quad (\text{A3})$$

$$C_l(\alpha) \geq C_l(x) \quad \forall x \in [\alpha - \delta, \alpha + \delta]$$

Note that this definition is more conservative than the typical definition of the stalling in practice, where flow at the rear region begins to fully separate and C_l is globally maximized. α_s is occasionally smaller than the global maximum of C_l . Nonetheless, this approach helps avoid overestimation of the stall angle, which is expected to happen in XFOIL because of the nature of its flow solver having a limited accuracy in stall and post-stall conditions.

CLD and α_s have been typically considered to be significant to characterize the airfoil performance. For example, when it comes to lift-type wind turbines, the point where CLD is maximized may be commonly chosen as the design point. Since a wind turbine cannot always operate in the design condition, however, α_s needs to be additionally considered to evaluate how far the turbines run under an increasing-lift condition. For well-designed airfoils, α_s generally occurs later than the design point, which yields tolerance in operation beyond the design point. Consequently, the stall angle tolerance, i.e. the range between these two angles of attack $\Delta\alpha$, which is expressed as

$$\Delta\alpha \equiv \max\left(0, \alpha_s - \underset{\alpha \in \mathbb{R}}{\operatorname{argmax}} CLD(\alpha)\right), \quad (\text{A4})$$

can be a proper choice to evaluate the off-design performance [82]. Figure 11 depicts a scheme of how CLD and $\Delta\alpha$ are determined on performance curves of an airfoil.

Appendix B: Baseline Airfoil Shapes and Validation

Our optimization methodology does not rely on one specific airfoil evaluation tool. To compare our results with the previous literature and to help future researchers quickly reproduce our results, we use XFOIL[42] in the present study. The two design objectives, CLD_{max} and $\Delta\alpha$, are obtained from the C_l and C_d data calculated by the XFOIL at different angle of attacks (see Figure 11).

To achieve better efficiency and consistency, we only use the XFOIL to generate the performance data and do not use any of its built-in paneling features. The conditioning and the re-paneling of the morphed airfoil coordinates are handled at the end of our DbM

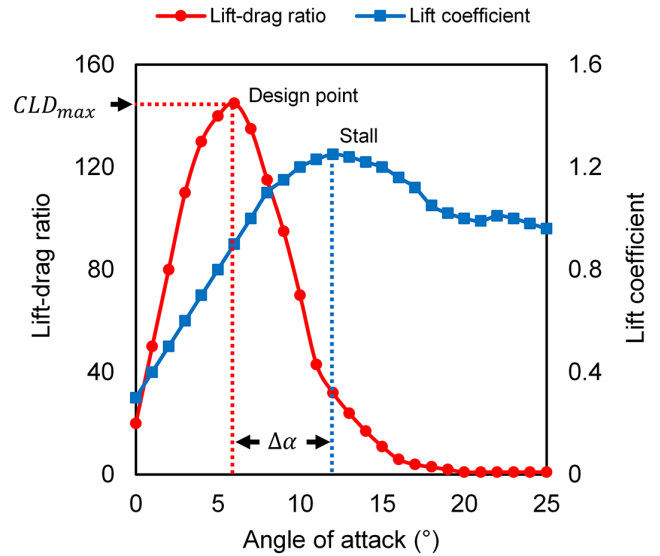


Fig. 11 Airfoil performance curves

algorithm. To reduce the evaluation time, we perform a rough scan first with an α increment of 1° and then finer scans for CLD_{max} and $\Delta\alpha$ separately with an α increment of 0.25° .

It is worth noting that XFOIL uses a global Newton's method[42] to simultaneously solve for the boundary layer and the transition equations, and it uses the solution at the previous angle of attack as the starting guess. As a result, ill-conditioned airfoil coordinates and the occurrence of the flow separation can both lead to the non-convergence of the XFOIL evaluation. To ensure the robustness and correctness of our airfoil evaluation, our XFOIL wrapper attempts to reach convergence by re-starting the root-finding with a fresh starting guess and by gradually increasing the number of the panels. If both attempts fail, the wrapper will check the convergence at the neighboring points, which will indicate whether the flow separation occurs or not. Besides the non-convergence issue, we further verify the correctness of the Newton's method by comparing the calculated viscous drag coefficient and the inviscid drag coefficient, the later of which is determined purely by the potential flow theorem and have to be smaller than its viscous counterpart due to its negligence of the friction (viscous effect). Any angle with incorrect result will undergo the same treatment as the non-converging ones, hence ensuring the correctness of our airfoil performance evaluation. A comparison between our XFOIL evaluation and the past experimental results of the same airfoil under the same flow conditions is provided in the table.

Appendix C: Optimization Test Functions and Validation

We use the multi-objective problems, suggested by Zeidler et al.[80], for testing our GA setup. The details of the test functions are given in Table 2. All the test functions were minimized with 25 variables in the design space.

MATLAB's NSGA-II genetic algorithm, a fast sorting and elitist multi-objective genetic algorithm, was used in the current study. Single objective optimization for each objective and random sampling were used for initialization. The population size of 372 was used with a total of 3,000 maximum generations. A 'phenotype' crowding distance metric was used. This setup was validated on the test functions described above. All the problems were benchmarked with 25 variables ($d = 25$) and two objective functions ($K = 2$) as with the present airfoil optimization problem. The results of our setup on four benchmark problems are shown in

Table 1 The model names, features, shape outlines, and XFOIL evaluation results of the 25 baseline shapes used by DbM in this paper. The coordinates of the baseline shapes are obtained from the UIUC airfoil coordinates database[38]. The airfoil evaluation results are obtained for an incompressible outer-flow of $Re = 1 \times 10^6$. The reference evaluation results are interpolated from the Airfoil Tools online database[83], where N/A indicates that there is no data available for this airfoil.


























Index	Model Name	Series (Features)	Airfoil Shape	Reference[83]		Present	
				CLD_{max}	$\Delta\alpha$	CLD_{max}	$\Delta\alpha$
1	NACA 0012	NACA (4-digit)		75.6	8.50	69.3	6.75
2	NACA 2412	NACA (4-digit)		101.4	12.00	99.5	12.00
3	NACA 4412	NACA (4-digit)		129.4	1.75	126.2	11.50
4	E 205	Eppler		128.3	8.50	124.4	10.50
5	AH 81-K-144 W-F Klappe	Althaus		89.7	2.00	91.6	2.00
6	AH 79-100 C	Althaus		183.0	14.75	170.6	15.50
7	AH 79-K-143/18	Althaus		110.9	1.50	107.0	1.50
8	AH 94-W-301	Althaus		103.0	4.00	101.4	2.75
9	NACA 23112	NACA (5-digit)		98.6	6.75	96.9	8.00
10	NACA 64(2)-415	NACA (6-digit)		120.6	12.50	113.8	13.00
11	NACA 747(A)-315	NACA (7-digit)		111.5	12.00	105.8	13.00
12	Griffith 30% Suction	Griffith (Suction)		17.3	0.00	17.9	0.00
13	AS 6097	Selig (Bird-like)		N/A	N/A	171.2	14.00
14	E 379	Eppler (Bird-like)		N/A	N/A	160.0	2.00
15	Clark YS	Clark		85.7	5.25	82.3	5.75
16	Clark W	Clark		116.1	11.00	114.8	11.00
17	Clark Y	Clark		114.8	11.75	113.7	12.75
18	Chen	Chen		125.4	0.00	126.7	0.00
19	S2027 Flipped	Selig (Flipped)		N/A	N/A	0.00	0.00
20	GOE 417A	Gottingen (Thin plate)		86.7	5.25	90.4	5.25
21	GOE 611	Gottingen (Flat bottom)		125.6	9.00	129.7	9.00
22	Dragonfly Canard	Dragonfly		144.6	2.50	147.5	3.00
23	FX 79-W-470A	Wortmann (Fat)		N/A	N/A	23.9	9.25
24	Sikorsky DBLN-526	Sikorsky (Fat)		53.3	4.75	51.5	4.25
25	FX 82-512	Wortmann		99.1	14.75	98.7	13.00

Figure 12. It was found that the algorithm could capture $ZDT1$, $ZDT2$, and $ZDT4$ accurately and predicts $ZDT6$, which is not only non-convex but also non-uniform, reasonably well.

Appendix D: Airfoil Shape Clustering

To analyze characteristics of the optimized airfoil shapes in detail, the airfoil shapes on the Pareto front are classified into 3 clusters using k -means clustering based on the Euclidean distance with $k = 3$. The clustering is performed in the design variable space, or weight space, of \mathcal{D}^{25} rather than in the objective plane because the purpose of clustering is to identify common geometric features over different airfoil shapes as a result of the optimization. The selection of the cluster size is based on the PCA of the optimal weight vector set.

Figure 13 shows the projection of the 25-dimensional weight vector set to the 2-dimensional subspace spanned by 2 PCA axes having the first- and second-most variance. The explained variance ratios of PCA axes 1 and 2 are 77.8% and 14.6%, respectively. On the other hand, the PCA axis of the third-most variance accounts for only 2.5% of the variance, affirming that the 2-dimensional projection in Figure 13 adequately scatters the clusters. From this observation, $k = 3$ is thought to be the most appropriate cluster size.

Table 2 Benchmark Test Functions. All of the test functions are bi-objective with extended to n -dimensional constrained search space.

Problem	Bounds	Objective Functions	Optima	Note
ZDT1	$w_i \in [0, 1],$ $i = 1, \dots, n$	$f_1(\mathbf{w}) = w_1$ $f_2(\mathbf{w}) = g(\mathbf{w}) \left[1 - (f_1(\mathbf{w})/g(\mathbf{w}))^{1/2} \right]$ $g(\mathbf{w}) = 1 + 9 \left(\sum_{i=2}^n w_i \right) / (n-1)$	$w_1 \in [0, 1]$ $w_i = 0,$ $i = 2, \dots, n$	convex
ZDT2	$w_i \in [0, 1],$ $i = 1, \dots, n$	$f_1(\mathbf{w}) = w_1$ $f_2(\mathbf{w}) = g(\mathbf{w}) \left[1 - (f_1(\mathbf{w})/g(\mathbf{w}))^2 \right]$ $g(\mathbf{w}) = 1 + 9 \left(\sum_{i=2}^n w_i \right) / (n-1)$	$w_1 \in [0, 1]$ $w_i = 0,$ $i = 2, \dots, n$	non-convex
ZDT4	$w_1 \in [0, 1]$ $w_i \in [-5, 5],$ $i = 2, \dots, n$	$f_1(\mathbf{w}) = w_1$ $f_2(\mathbf{w}) = g(\mathbf{w}) \left[1 - (f_1(\mathbf{w})/g(\mathbf{w}))^{1/2} \right]$ $g(\mathbf{w}) = 10n + \sum_{i=2}^n (w_i^2 - 10 \cos(4\pi w_i)) - 9$	$w_1 \in [0, 1]$ $w_i = 0,$ $i = 2, \dots, n$	non-convex
ZDT6	$w_i \in [0, 1],$ $i = 1, \dots, n$	$f_1(\mathbf{w}) = 1 - \exp(-4w_1) \sin^6(6\pi w_1)$ $f_2(\mathbf{w}) = g(\mathbf{w}) \left[1 - (f_1(\mathbf{w})/g(\mathbf{w}))^2 \right]$ $g(\mathbf{w}) = 1 + 9 \left[\left(\sum_{i=2}^n w_i \right) / (n-1) \right]^{1/4}$	$w_1 \in [0, 1]$ $w_i = 0,$ $i = 2, \dots, n$	non-convex, non-uniform

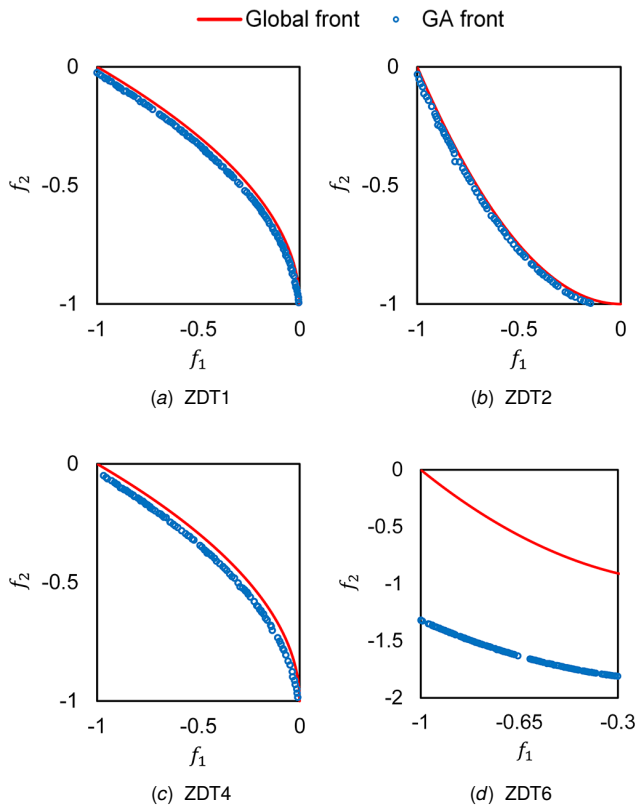


Fig. 12 Multi-objective optimization of benchmark test functions using GA

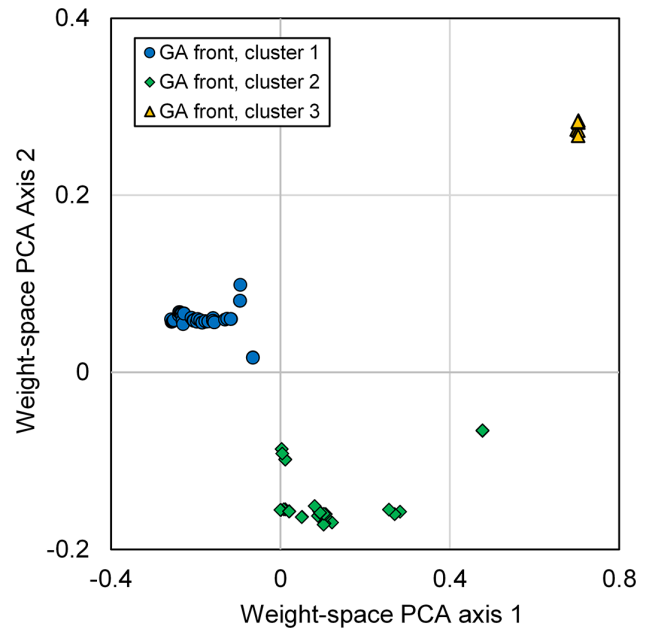


Fig. 13 Projection of the 25-dimensional optimal weight vectors to the 2-dimensional subspace spanned by 2 PCA axes of the dominant variance. k -means clustering with the cluster size of 3 is used to identify the clusters.

References

- [1] Drela, M., *Pros & Cons of Airfoil Optimization*, pp. 363–381.
- [2] Besnard, E., Schmitz, A., Boscher, E., Garcia, N., and Cebeci, T., 1998, “Two-dimensional aircraft high lift system design and optimization,” *36th AIAA Aerospace Sciences Meeting and Exhibit*.
- [3] Vicini, A. and Quagliarella, D., 1999, “Airfoil and Wing Design Through Hybrid Optimization Strategies,” *AIAA Journal*, **37**(5), p. 634–641.
- [4] Elham, A. and van Tooren, M. J., 2014, “Winglet multi-objective shape optimization,” *Aerospace Science and Technology*, **37**, p. 93–109.
- [5] Li, J.-Y., Li, R., Gao, Y., and Huang, J., 2010, “Aerodynamic optimization of wind turbine airfoils using response surface techniques,” *Proceedings of the Institution of Mechanical Engineers, Part A: Journal of Power and Energy*, **224**(6), p. 827–838.
- [6] Ju, Y. P. and Zhang, C. H., 2011, “Multi-point robust design optimization of wind turbine airfoil under geometric uncertainty,” *Proceedings of the Institution of Mechanical Engineers, Part A: Journal of Power and Energy*, **226**(2), p. 245–261.
- [7] Ribeiro, A., Awruch, A., and Gomes, H., 2012, “An airfoil optimization technique for wind turbines,” *Applied Mathematical Modelling*, **36**(10), p. 4898–4907.
- [8] Grasso, F., 2012, “Hybrid Optimization for Wind Turbine Thick Airfoils,” *53rd AIAA/ASME/ASCE/AHS/ASC Structures, Structural Dynamics and Materials Conference
20th AIAA/ASME/AHS Adaptive Structures Conference
14th AIAA*.
- [9] Chehouri, A., Younes, R., Ilincă, A., and Perron, J., 2015, “Review of performance optimization techniques applied to wind turbines,” *Applied Energy*, **142**, p. 361–388.
- [10] Ali, Q. S. and Kim, M.-H., 2021, “Design and performance analysis of an air-borne wind turbine for high-altitude energy harvesting,” *Energy*, **230**, p. 120829.
- [11] Sobester, A. and Barrett, T., 2008, “Quest for a Truly Parsimonious Airfoil Parameterization Scheme,” *The 26th Congress of ICAS and 8th AIAA ATIO*.
- [12] Sripawadkul, V., Padulo, M., and Guenov, M., 2010, “A Comparison of Airfoil Shape Parameterization Techniques for Early Design Optimization,” *13th AIAA/ISSMO Multidisciplinary Analysis Optimization Conference*, American Institute of Aeronautics and Astronautics, Fort Worth, Texas, doi: [10.2514/6.2010-9050](https://doi.org/10.2514/6.2010-9050).
- [13] Masters, D. A., Taylor, N. J., Rendall, T., Allen, C. B., and Poole, D. J., 2015, “Review of Aerofoil Parameterisation Methods for Aerodynamic Shape Optimisation,” *53rd AIAA Aerospace Sciences Meeting*, American Institute of Aeronautics and Astronautics, Kissimmee, Florida, doi: [10.2514/6.2015-0761](https://doi.org/10.2514/6.2015-0761).
- [14] Jameson, A., 1988, “Aerodynamic design via control theory,” *Journal of Scientific Computing*, **3**(3), p. 233–260.
- [15] Samareh, J. A., 2001, “Survey of Shape Parameterization Techniques for High-Fidelity Multidisciplinary Shape Optimization,” *AIAA Journal*, **39**(5), p. 877–884.
- [16] Sobieczky, H., 1999, “Parametric Airfoils and Wings,” *Recent Development of Aerodynamic Design Methodologies*, E. H. Hirschel, K. Fujii, W. Haase, B. van Leer, M. A. Leschziner, M. Pandolfi, A. Rizzi, B. Roux, K. Fujii, and G. S. Dulikravich, eds., Vol. 65, Vieweg+Teubner Verlag, Wiesbaden, pp. 71–87.
- [17] Farin, G., 1993, “Chapter 4 - The Bernstein Form of a Bézier Curve,” *Curves and Surfaces for Computer-Aided Geometric Design (Third Edition)*, Third edition ed., G. Farin, ed., Academic Press, Boston, pp. 41–63.
- [18] Rogalsky, T. and Derksen, R. W., 2009, “Bézier-PARSEC parameterization for airfoil optimization,” *Canadian Aeronautics and Space Journal*, **55**(3), pp. 163–174.
- [19] Sanaye, S. and Hassanzadeh, A., 2014, “Multi-objective optimization of airfoil shape for efficiency improvement and noise reduction in small wind turbines,” *Journal of Renewable and Sustainable Energy*, **6**(5), p. 053105.
- [20] Han, X. and Zingg, D. W., 2014, “An adaptive geometry parameterization for aerodynamic shape optimization,” *Optimization and Engineering*, **15**(1), pp. 69–91.
- [21] Schramm, U., Pilkey, W. D., DeVries, R. I., and Zebrowski, M. P., 1995, “Shape design for thin-walled beam cross sections using rational B splines,” *AIAA Journal*, **33**(11), p. 2205–2211.
- [22] Sederberg, T. W. and Parry, S. R., 1986, “Free-form deformation of solid geometric models,” *ACM SIGGRAPH Computer Graphics*, **20**(4), p. 151–160.
- [23] Lamouin, H. and Waggenspack, N., 1994, “NURBS-based free-form deformations,” *IEEE Computer Graphics and Applications*, **14**(6), p. 59–65.
- [24] Wendland, H., 2004, “Scattered Data Approximation,”
- [25] Buhmann, M. D., 2003, “Radial Basis Functions,”
- [26] J. Toal, D. J., Bressloff, N. W., Keane, A. J., and E. Holden, C. M., 2010, “Geometric Filtration Using Proper Orthogonal Decomposition for Aerodynamic Design Optimization,” *AIAA Journal*, **48**(5), p. 916–928.
- [27] Ghoman, S., Wang, Z., Chen, P., and Kapania, R., 2012, “A POD-based Reduced Order Design Scheme for Shape Optimization of Air Vehicles,” *53rd AIAA/ASME/ASCE/AHS/ASC Structures, Structural Dynamics and Materials Conference
20th AIAA/ASME/AHS Adaptive Structures Conference
14th AIAA*.
- [28] Hicks, R. M. and Henne, P. A., 1978, “Wing Design by Numerical Optimization,” *Journal of Aircraft*, **15**(7), pp. 407–412.
- [29] Kulfan, B. and Bussoletti, J., 2006, “Fundamental” Parametric Geometry Representations for Aircraft Component Shapes,” *11th AIAA/ISSMO Multidisciplinary Analysis and Optimization Conference*, American Institute of Aeronautics and Astronautics, Portsmouth, Virginia, doi: [10.2514/6.2006-6948](https://doi.org/10.2514/6.2006-6948).
- [30] Akram, M. T. and Kim, M.-H., 2021, “CFD Analysis and Shape Optimization of Airfoils Using Class Shape Transformation and Genetic Algorithm—Part I,” *Applied Sciences*, **11**(9), p. 3791.
- [31] Viswanath, A., Forrester, A. I. J., and Keane, A. J., 2011, “Dimension Reduction for Aerodynamic Design Optimization,” *AIAA Journal*, **49**(6), p. 1256–1266.
- [32] Viswanath, A., Forrester, A. I. J., and Keane, A. J., 2014, “Constrained Design Optimization Using Generative Topographic Mapping,” *AIAA Journal*, **52**(5), p. 1010–1023.
- [33] Cinquegrana, D. and Iuliano, E., 2018, “Investigation of adaptive design variables bounds in dimensionality reduction for aerodynamic shape optimization,” *Computers & Fluids*, **174**, p. 89–109.
- [34] Chen, W., Chiu, K., and Fuge, M. D., 2020, “Airfoil Design Parameterization and Optimization Using Bézier Generative Adversarial Networks,” *AIAA Journal*, **58**(11), p. 4723–4735.
- [35] Oh, S., Jiang, C.-H., Jiang, C., and Marcus, P. S., 2018, “Finding the optimal shape of the leading-and-trailing car of a high-speed train using design-by-morphing,” *Computational Mechanics*, **62**(1), pp. 23–45.
- [36] Sheikh, H. M. and Marcus, P. S., 2019, “Vertical Axis Wind Turbine Design Using Design-by-Morphing and Bayesian Optimization,” *APS Division of Fluid Dynamics Meeting Abstracts*, p. Q14.007.
- [37] Koroglu, S. M. and Ozkol, I., 2019, “optimization of an Airfoil Characteristics to Minimize the Turn Radius of a Small Unmanned Aerial Vehicle,” *2019 IEEE 10th International Conference on Mechanical and Aerospace Engineering (ICMAE)*.
- [38] Selig, M. S., 1996, “UIUC Airfoil Data Site,” Last access: Feb 2022, <https://m-selig.ae.illinois.edu/ads.html>
- [39] Piotrowski, M. G. and Zingg, D. W., 2022, “Investigation of a Smooth Local Correlation-based Transition Model in a Discrete-Adjoint Aerodynamic Shape Optimization Algorithm,” *AIAA SCITECH 2022 Forum*.
- [40] He, X., Li, J., Mader, C. A., Yildirim, A., and Martins, J. R., 2019, “Robust aerodynamic shape optimization—From a circle to an airfoil,” *Aerospace Science and Technology*, **87**, p. 48–61.
- [41] Kenway, G. K. W. and Martins, J. R. R. A., 2016, “Multipoint Aerodynamic Shape Optimization Investigations of the Common Research Model Wing,” *AIAA Journal*, **54**(1), p. 113–128.
- [42] Drela, M., 1989, “XFoil: An Analysis and Design System for Low Reynolds Number Airfoils,” *Lecture Notes in Engineering*, p. 1–12.
- [43] Ronsten, G., 1992, “Static pressure measurements on a rotating and a non-rotating 2.375 m wind turbine blade. Comparison with 2D calculations,” *Journal of Wind Engineering and Industrial Aerodynamics*, **39**(1-3), p. 105–118.
- [44] Gigue' re, P. and Selig, M. S., 1998, “New Airfoils for Small Horizontal Axis Wind Turbines,” *Journal of Solar Energy Engineering*, **120**(2), p. 108–114.
- [45] Jones, B. R., Crossley, W. A., and Lyrintzis, A. S., 2000, “Aerodynamic and Aeroacoustic Optimization of Rotorcraft Airfoils via a Parallel Genetic Algorithm,” *Journal of Aircraft*, **37**(6), p. 1088–1096.
- [46] Mueller, T. J. and DeLaurier, J. D., 2003, “AERODYNAMICS OF SMALL VEHICLES,” *Annual Review of Fluid Mechanics*, **35**(1), p. 89–111.
- [47] Johnson, F. T., Tinoco, E. N., and Yu, N. J., 2005, “Thirty years of development and application of CFD at Boeing Commercial Airplanes, Seattle,” *Computers & Fluids*, **34**(10), p. 1115–1151.
- [48] Batten, W., Bahaj, A., Molland, A., and Chaplin, J., 2006, “Hydrodynamics of marine current turbines,” *Renewable Energy*, **31**(2), p. 249–256.
- [49] Lafountain, C., Cohen, K., and Abdallah, S., 2010, “Use of XFoil in design of camber-controlled morphing UAVs,” *Computer Applications in Engineering Education*, **20**(4), p. 673–680.
- [50] Ramanujam, G. and Ozdemir, H., 2017, “Improving Airfoil Lift Prediction,” *35th Wind Energy Symposium*.
- [51] Robert J. McGhee, B. S. W., 1988, “experimental results for the eppler 387 airfoil at low reynolds numbers in the langley low-turbulence pressure tunnel.”
- [52] Selig, M. S., 1995, *Summary of low speed airfoil data. Vol. 1*, Virginia Beach, Va. Soartech Publications.
- [53] Morgado, J., Vizinho, R., Silvestre, M., and Páscoa, J., 2016, “XFoil vs CFD performance predictions for high lift low Reynolds number airfoils,” *Aerospace Science and Technology*, **52**, p. 207–214.
- [54] Kaisa, M., 1999, *Nonlinear Multiobjective Optimization*, Vol. 12 of International Series in Operations Research & Management Science, Kluwer Academic Publishers, Boston, USA.
- [55] Gunantara, N., 2018, “A review of multi-objective optimization: Methods and its applications,” *Cogent Engineering*, **5**(1), p. 1502242.
- [56] Barron F. H., B. B. E., 1996, “Decision quality using ranked attribute weights,” *Management Science*, **42**, p. 1515.
- [57] Das I., D. J. E., 1997, “A closer look at drawbacks of minimizing weighted sums of objectives for Pareto set generation in multi-criteria optimization problems,” *Structural Optimization*, **14**, p. 63.
- [58] T. C. C., 2007, “Multi-choice goal programming,” *Omega*, **35**, p. 389.
- [59] Ghachi, R. F., Alnahhal, W. I., Abdeljaber, O., Renno, J., Tahidul Haque, A. B. M., Shim, J., and Aref, A., 2020, “Optimization of Viscoelastic Metamaterials for Vibration Attenuation Properties,” *International Journal of Applied Mechanics*, **12**(10), p. 2050116.
- [60] Vangelatos, Z., Sheikh, H. M., Marcus, P. S., Grigoropoulos, C. P., Lopez, V. Z., Flamourakis, G., and Farsari, M., 2021, “Strength through defects: A novel Bayesian approach for the optimization of architected materials,” *Science Advances*, **7**(41), p. eabk2218.
- [61] Schlieter, T. and Dlugosz, A., 2020, “STRUCTURAL OPTIMIZATION OF AEROFOILS FOR MANY CRITERIA,” pp. 448–451, doi: [10.2514/6.2020-448](https://doi.org/10.2514/6.2020-448).

- [62] Xu, B., Li, Z., Zhu, Z., Cai, X., Wang, T., and Zhao, Z., 2021, "The Parametric Modeling and Two-Objective Optimal Design of a Downwind Blade," *Frontiers in Energy Research*, **9**, p. 432.
- [63] Chehour, A., Younes, R., Ilinca, A., and Perron, J., 2016, "Wind Turbine Design: Multi-Objective Optimization," *Wind Turbines - Design, Control and Applications*.
- [64] Rodrigues, S., Bauer, P., and Bosman, P. A., 2016, "Multi-objective optimization of wind farm layouts – Complexity, constraint handling and scalability," *Renewable and Sustainable Energy Reviews*, **65**, pp. 587–609.
- [65] Wang, X. D., Hirsch, C., Kang, S., and Lacor, C., 2011, "Multi-objective optimization of turbomachinery using improved NSGA-II and approximation model," *Computer Methods in Applied Mechanics and Engineering*, **200**(9-12), pp. 883–895.
- [66] Nguyen, P., 2021, "A review of Hybrid/combined methods for trajectory optimization of flight vehicles," *Journal of Physics: Conference Series*, **1958**(1), p. 012032.
- [67] Gao, H., Zhang, Y., Zhou, X., and Li, D., 2018, "Intelligent methods for the process parameter determination of plastic injection molding," *Frontiers of Mechanical Engineering*, **13**(1), 85 (10 pages).
- [68] Wang, D., Geng, L., Zhao, Y.-J., Yang, Y., Huang, Y., Zhang, Y., and Shen, H.-B., 2019, "Artificial intelligence-based multi-objective optimization protocol for protein structure refinement," *Bioinformatics*, **36**(2), pp. 437–448.
- [69] Li, Y., Wei, K., Yang, W., and Wang, Q., 2020, "Improving wind turbine blade based on multi-objective particle swarm optimization," *Renewable Energy*, **161**, pp. 525–542.
- [70] Franco Correia, V., Moita, J. S., Moleiro, F., and Soares, C. M. M., 2021, "Optimization of Metal–Ceramic Functionally Graded Plates Using the Simulated Annealing Algorithm," *Applied Sciences*, **11**(2).
- [71] Ciardiello, A., Rosso, F., Dell'Olmo, J., Ciancio, V., Ferrero, M., and Salata, F., 2020, "Multi-objective approach to the optimization of shape and envelope in building energy design," *Applied Energy*, **280**, p. 115984.
- [72] Fox, A. D., Corne, D. W., Mayorga Adame, C. G., Polton, J. A., Henry, L.-A., and Roberts, J. M., 2019, "An Efficient Multi-Objective Optimization Method for Use in the Design of Marine Protected Area Networks," *Frontiers in Marine Science*, **6**, p. 17.
- [73] Afshari, H., Hare, W., and Tesfamariam, S., 2019, "Constrained multi-objective optimization algorithms: Review and comparison with application in reinforced concrete structures," *Applied Soft Computing*, **83**, p. 105631.
- [74] Gao, Y., Shi, L., and Yao, P., 2000, "Study on multi-objective genetic algorithm," *Proceedings of the 3rd World Congress on Intelligent Control and Automation (Cat. No.00EX393)*, Vol. 1, pp. 646–650 vol.1, doi: [10.1109/WCICA.2000.860052](https://doi.org/10.1109/WCICA.2000.860052).
- [75] Skinner, S. and Zare-Behtash, H., 2018, "State-of-the-art in aerodynamic shape optimisation methods," *Applied Soft Computing*, **62**, pp. 933–962.
- [76] Rahmad, Y., Robani, M. D., Palar, P. S., and Zuhul, L. R., 2020, "Single- and multi-objective optimization of a low-speed airfoil using genetic algorithm," *Tangerang Selatan, Indonesia*, p. 020005, doi: [10.1063/5.0002610](https://doi.org/10.1063/5.0002610).
- [77] Zhao, K., Gao, Z., and tao Huang, J., 2014, "Robust design of natural laminar flow supercritical airfoil by multi-objective evolution method," *Applied Mathematics and Mechanics*, **35**, pp. 191–202.
- [78] Sheikh, H. M. and Marcus, P. S., 2022, "Bayesian Optimization For Multi-Objective Mixed-Variable Problems," [2201.12767](https://arxiv.org/abs/2201.12767), <http://arxiv.org/abs/2201.12767>
- [79] Deb, K., Pratap, A., Agarwal, S., and Meyarivan, T., 2002, "A fast and elitist multiobjective genetic algorithm: NSGA-II," *IEEE Transactions on Evolutionary Computation*, **6**(2), pp. 182–197.
- [80] Zitzler, E., Deb, K., and Thiele, L., 2000, "Comparison of Multiobjective Evolutionary Algorithms: Empirical Results," *Evol. Comput.*, **8**(2), p. 173–195.
- [81] Ananda, G. K. and Selig, M. S., 2018, "Design of bird-like airfoils," *2018 AIAA Aerospace Sciences Meeting*, p. 0310.
- [82] Li, X., Yang, K., Bai, J., and Xu, J., 2013, "A method to evaluate the overall performance of the CAS-W1 airfoils for wind turbines," *Journal of Renewable and Sustainable Energy*, **5**(6), p. 063118.
- [83] 2022, "Airfoil database search," Last access: May 2022, <http://airfoiltools.com/>

List of Figures

1	An example of DbM. The coordinates of the baseline shapes are weighted, summed, and normalized to form the coordinates of a morphed shape.	2
	(a) n^{th} airfoil shape	2
	(b) y -coordinate collocation vector	2
2	An Example of DbM. Column 1 shows the baseline shapes. Column 2 depicts the elements of the collocation vectors of the baseline shapes plotted as a function of the index i of the collocation vector. Column 3 shows the weighted elements of the collocation vector plotted as a function of the index i of the collocation vector. Column 4 shows the resultant collocation vector of the morphed shape and the morphed shape itself.	3
3	Conditioning for intersection removal. (a) Intersections are detected; (b) Blown up image of one intersection. Shape coordinates direction is depicted by arrows; (c) Intersection removed by flipping vector between intersection; (d) Zero area removed by linear interpolation to remove the intersecting area and then smoothed over, shown by hat coordinates	4
	(a)	4
	(b)	4
	(c)	4
	(d)	4
4	Twenty-five baseline shapes picked from the UIUC airfoil coordinates database[38]. See Appendix B for more details.	4
5	Reconstruction of randomly chosen 100 pre-existing airfoil shapes via DbM using twenty-five baseline shapes in Figure 4.	5
6	General flowchart of airfoil optimization via DbM	5
7	The Pareto front consisting of the optimal airfoil shapes as a result of the 3,000 generation runs of NSGA-II. Twenty-five red hollow circles with indices indicate twenty-five baseline airfoil shape evaluations. See Appendix D to understand how the clustering is performed.	6
8	Nine representative Pareto-optimal airfoil shapes. (a)-(c) are in cluster 1, (d)-(f) are in cluster 2 and (g)-(i) are in cluster 3.	7
	(a)	7
	(b)	7
	(c)	7
	(d)	7
	(e)	7
	(f)	7
	(g)	7
	(h)	7
	(i)	7
9	Mean weight distributions of the Pareto-optimal airfoil shapes with respect to twenty-five baseline airfoil shapes.	8
10	Morphed airfoil shapes generated by the optimal weight vectors, representing (a) the total mean of all optimal airfoils' weights, (b) the coefficients of the PCA axis having the most variance and (c) the coefficients of the PCA axis having the second-most variance. The black and red surfaces correspond to the first and second half of the collocation points, respectively.	8
	(a) Total mean	8
	(b) PCA axis 1	8
	(c) PCA axis 2	8
11	Airfoil performance curves	9
12	Multi-objective optimization of benchmark test functions using GA	11
	(a) ZDT1	11
	(b) ZDT2	11
	(c) ZDT4	11
	(d) ZDT6	11
13	Projection of the 25-dimensional optimal weight vectors to the 2-dimensional subspace spanned by 2 PCA axes of the dominant variance. k -means clustering with the cluster size of 3 is used to identify the clusters.	11

List of Tables

1	The model names, features, shape outlines, and XFOIL evaluation results of the 25 baseline shapes used by DbM in this paper. The coordinates of the baseline shapes are obtained from the UIUC airfoil coordinates database[38]. The airfoil evaluation results are obtained for an incompressible outer-flow of $Re = 1 \times 10^6$. The reference evaluation results are interpolated from the Airfoil Tools online database[83], where N/A indicates that there is no data available for this airfoil.	10
2	Benchmark Test Functions. All of the test functions are bi-objective with extended to n -dimensional constrained search space.	11